




Article

Effect of Fe Concentration and Superheating on the Microstructure and Tensile Properties of High Mg 413.0-Type Alloys: Role of Sr, Be, P, and La

Herbert W. Doty¹, Ehab Samuel², Agnes M. Samuel², Ehab Elsharkawi³ , Victor Songmene⁴ 
and Fawzy H. Samuel^{2,*} 

¹ Materials Technology, General Motors Global Technology Center, Warren, MI 48092, USA; herb.doty@gm.com

² Département des Sciences Appliquées, Université du Québec à Chicoutimi, Saguenay, QC G7H 2B1, Canada; ehabfhsamuel@gmail.com (E.S.); agnesmsamuel@gmail.com (A.M.S.)

³ Division of Engineering, Saint Mary's University, Halifax, NS B3H 3C3, Canada; ehab.elsharkawi@smu.ca

⁴ Department of Mechanical Engineering, École de Technologie Supérieure, Montreal, QC H3C 1K3, Canada; victor.songmene@etsmtl.ca

* Correspondence: fawzy-hosny.samuel@etsmtl.ca

Abstract: The present work was undertaken to explore the multiple alloys and process steps that have been suggested to mitigate the harmful effects of high iron content in cast Al-Si alloys. The base alloy used was commercial 413.0 alloy containing 0.35%Mg. Iron was added at three Fe levels up to 1.8%. The addition of Sr, 1.0%Zn, 0.2%Ti were made to the alloys so prepared, which were melted and maintained at a superheat of 750 °C or 950 °C. The melts were poured in different molds that produced three solidification rates. In total, 40 castings were prepared: half of the castings were used for metallographic examinations in the as-cast condition, while the other half were set aside for tensile testing following T6 treatment. The results show that at a solidification rate of 50 °C/s, 1.8%Fe could be dissolved in the aluminum matrix regardless of other melt treatments. With regard to the other solidification rates, superheating at 950 °C, coupled with Sr addition or Sr + Be, reduces the average β -platelets length by 80% (0.8 °C/s) or 95% (8 °C/s). The addition of P causes a marked drop in the alloy tensile strength due to the precipitation of primary Si, Al₂Si₂Sr, and β -AlFeSi hard-phase particles. Therefore, reducing the iron content in the castings may be considered a major objective to be recommended for developing alloys with higher strength and optimum quality values. More than 1000 tensile bars were tested in this study.

Keywords: aluminum alloys; superheating; Fe content; Sr modification; Al₂Si₂Sr phase



Academic Editor: Shuncun Luo

Received: 20 November 2024

Revised: 12 December 2024

Accepted: 18 December 2024

Published: 8 January 2025

Citation: Doty, H.W.; Samuel, E.; Samuel, A.M.; Elsharkawi, E.; Songmene, V.; Samuel, F.H. Effect of Fe Concentration and Superheating on the Microstructure and Tensile Properties of High Mg 413.0-Type Alloys: Role of Sr, Be, P, and La. *Materials* **2025**, *18*, 249. <https://doi.org/10.3390/ma18020249>

Copyright: © 2025 by the authors. Licensee MDPI, Basel, Switzerland. This article is an open access article distributed under the terms and conditions of the Creative Commons Attribution (CC BY) license (<https://creativecommons.org/licenses/by/4.0/>).

1. Introduction

The harmful effects of certain metals, such as iron (Fe), which is found in 413 alloys (used in this project), constitute one of the main problems encountered in metallurgy. Indeed, a high percentage of iron promotes the precipitation of Fe phases, which especially reduces ductility [1–4]. Several authors have suggested the overheating pathway as a means to neutralize the harmful effects of iron without even adding neutralizing elements such as manganese (Mn) and/or chromium (Cr) [5,6]. Certain studies have shown the relationship between the overheating temperature and the iron phases formed, as well as the importance of maintaining low concentrations of such elements as Fe, Si, and Mg while applying a rapid solidification rate, to promote complete precipitation of iron in the form of the less harmful α -AlFeSi Chinese script phase [7,8].

The Al-Fe phase diagram shows a eutectic at the temperature of 655 °C at 1.8% Fe. This eutectic is formed by aluminum (Al) and the phase FeAl₃, with a maximum solubility of iron in aluminum of 0.052%. Under equilibrium conditions, the phases present in the solid state show a low solubility of silicon in aluminum when a small quantity of iron is added. Under non-equilibrium conditions, four phases can be encountered simultaneously: Al, Si, α -AlFeSi, and β -AlFeSi [9,10].

Intermetallic phases are generally categorized by three morphologies: polygonal crystals, Chinese script, and thin plates. Equilibrium diagrams of diluted Al-Fe-Si alloys include the Θ -AlFeSi (monoclinic) phase, the α -Al₃Fe₂Si (hexagonal) phase, the β -Al₅FeSi (monoclinic) phase, and the α -AlFeSi phase, whose chemical composition is Al₁₂Fe₃Si₂ (30.7% Fe, 10.2% Si) [8]. These phases dominate during slow cooling, and metastable phases like Al₆Fe (orthorhombic) and α -Al₂₀Fe₅Si₂ (cubic) are precipitated during quenching or rapid cooling. In several commercial aluminum alloys that contain Mn or Cr as an impurity, the cubic α -AlFeSi, rather than the hexagonal α -AlFeSi phase, is formed. It was observed that the β -AlFeSi phase precipitates during the liquid–solid (pre-eutectic) reaction, as well as during the formation of the eutectic (co-eutectic) reaction, when the iron concentration exceeds 0.7% [11–13].

Increasing the melting temperature (superheating) has been proposed to eliminate the β -AlFeSi intermetallic, which is harmful to the mechanical properties of aluminum alloys. Overheating transforms the β -AlFeSi phase into the Chinese script phase. Overheating and rapid solidification reduce the interdendritic space, the size of the constituents of the eutectic and first phases, and the grain size, despite the increase in real-time solidification [5]. Barlock and Mondolfo [14] add that aluminum alloys contain a germination catalyst (nucleation site), which acts at the zero-supercooling point, and when the overheating exceeds 500 °C, the size and possibly the number of germination particles are reduced but are not eliminated completely.

Crepeau [15] points out that superheating aluminum alloys increases the concentration of hydrogen and oxide inclusions in the molten metal. However, no mention is made of the type of alloy referred to by the author. The mechanism behind contamination of the molten alloy may explain the effect of neutralization and transformation of γ -alumina inclusions into α -alumina. Apparently, the β -AlFeSi phase nucleates on the fine γ -alumina inclusions but not the α -alumina phase [15].

Narayanan et al. [16,17] report that overheating is more effective in refining the α -AlFeSi phase than the addition of manganese in 319 alloys containing 1% iron. They showed overheating is useful not only in transforming the β -phase into Chinese script but also in reducing the size of the intermetallics. Beryllium (Be) is used in Al-Si alloys to reduce oxidation of liquid metal while considering the increase in magnesium (Mg) concentration, and it accelerates hardening processes when the alloy is heat-treated in the T6 condition [18,19]. In addition, beryllium provides alloy fluidity, which increases its castability, especially in the case of automotive alloys. In the presence of beryllium in Al-7% Si-0.3% Mg–0.6% Fe alloys, some authors have observed the formation of a new BeSiFe₂Al₈ phase, which has a polygonal shape or Chinese script form [20]. This new phase precipitates mainly within the α -aluminum dendrites, while the β -phase is observed in the interdendritic regions. However, beryllium is used in low concentrations (0.01–0.05%) due to its toxicity [21].

Large primary silicon crystals adversely affect the mechanical properties of Al-Si alloys. Considerable research has been done in an attempt to reduce the size of primary silicon crystals. It has been found that phosphorus (P), when incorporated into the molten metal, can reduce the size of the primary silicon substantially [22]. Phosphorus refining must be

conducted in the molten metal during the solidification process since there is no way to refine large primary silicon crystals once they have been formed after casting [23–26].

Magnesium (Mg) is often used in Al-Si alloys in concentrations ranging from 0.07% to 0.4% to improve the mechanical properties of these alloys through precipitation of the Mg_2Si phase. When magnesium is added to commercial alloy A319, the $\beta-Al_5FeSi$ phase transforms into the $\pi-Al_8Mg_3FeSi_6$ phase [26]. The increase in concentration of magnesium increases the volume fraction of this phase. Also, the addition of Mg produces a reduction in the temperature of the silicon eutectic reaction [27,28].

The present investigations were undertaken to focus on the effects of solidification rate and overheating on the microstructure and tensile properties of the hypereutectic alloy A413, taking into consideration the role of additives (Fe, Be, Sr, P, RE), and superheating (melting temperature ~ 950 °C) on the morphology of $\beta-Al_5FeSi$ platelets in the absence of Mn and/or Cr and how both the morphology and characteristics of Fe-intermetallics determine the tensile properties of high Mg (0.35%) 413 aluminum alloys [29,30]. The solidification rates selected correspond to dendrite arm spacings of (DAS) 80–90 μm , 15–20 μm , and 3–5 μm representing, respectively, sand (0.8 °C/s), permanent mold (8 °C/s), and die (50 °C/s) casting techniques [31].

2. Experimental Procedure

Different additive elements were incorporated in various combinations and proportions into the base 413.0 alloy, among them Mg, Fe, Be, RE (La), and Sr, which improve the tensile properties of the base alloy 413.0. Additionally, phosphorus (P) was added for refining the primary silicon phase. The alloy was melted in a 28 kg capacity silicon carbide crucible using an electric furnace. The temperature of the metal was brought to ~ 735 °C and was maintained for the remainder of the melting procedure, including the addition of the various alloying elements, strontium modification, grain refinement, and degassing. Subsequently, the liquid metal was degassed by an injection of pure argon. Chemical analysis was conducted at three different stages for each alloy cast in order to establish a representative concentration sampling of all the elements present in the molten metal. Other batches of liquid metal were superheated at 950 °C for 30 min and then cooled to 735 °C, followed by degassing as above.

The strontium was added in the form of the Al-10% Sr master alloy, whereas the Al-5%Ti-1%B master alloy was used to add titanium diboride. Iron, Be, and P were added in the form of Al-25%Fe, Al-5%Be, and Cu-2%P master alloys, whereas La was added in the form of Al-50%La (using La 99.9% purity). Magnesium and zinc (Zn) were added as pure metals using a perforated graphite bell. Degassing of the liquid metal, when necessary, is done with a rotary graphite stirrer, which rotates at a speed of 150 rpm, and which passes pure dry argon at a flow rate of 0.492 cubic meters per hour for 30 min.

Table 1 lists the chemical composition of the as-received ingots. Two sets of castings were made, one for metallographic investigation of the alloys in the as-cast condition, while the second set was used for tensile testing. As for Be, Mg, and La, due to their high oxidation rate, the initial value was 50% higher than the aimed value to balance the weight loss. It should be emphasized here that Sr, Be, Mg, and La were added when the temperature of the molten metal was about 750 °C, 5 min before the end of degassing i.e., prior to casting. The chemical analysis was conducted using a Spectrolab-JrCCD Spark Analyzer (SPECTRO Analytical Instruments Inc., Mahwah, NJ, USA). The average chemical compositions (three burns per alloy sample) are reported in Table 2. Table 3 lists the chemical compositions of the selected alloys that were used for tensile testing. All alloys were grain-refined with 0.2% Ti in the form of the Al-5%Ti-1%B master alloy.

Table 1. Chemical composition of as received ingots of 413.0 alloy (coded E0).

Alloy	Elements (wt.%)									
	Si	Fe	Cu	Mn	Mg	Cr	Ti	Be	Sr	Al
E0-1	10.47	0.3801	0.4734	0.2374	0.0410	0.0302	0.0431	0.0006	0.000	87.8
E0-2	10.69	0.3561	0.4968	0.2462	0.0487	0.0291	0.0645	0.0002	<0.0000	87.8
E0-3	10.87	0.3593	0.4972	0.2424	0.0477	0.0295	0.0648	0.0002	0.0001	87.7

Table 2. Compositions of alloys prepared for metallographic examination.

Code	Description
EFHG EFPHG EFSHG EFBSHG	EF * alloy, super heating, graphite mold EF alloy + 30 ppm P, super heat, graphite mold EF alloy + 195 ppm Sr, super heat, graphite mold EF alloy + 195 ppm Sr + 500 ppm Be, super heat, graphite mold
EFHM EFPHM EFSHM EFBSHM EFTHM EFZHM EFTZHM EFSLHM	EF * alloy, super heating, metallic mold EF alloy + 30 ppm P, super heat, metallic mold EF alloy + 195 ppm Sr, super heat, metallic mold EF alloy + 195 ppm Sr + 500 ppm Be, super heat, metallic mold EF alloy + 0.2%Ti, super heat, metallic mold EF alloy + 1%Zn, super heat, metallic mold EF alloy + 1%Zn + 0.2%Ti, super heat, metallic mold EF alloy + 195 ppm Sr + 0.5%La, super heat, metallic mold
EFHC EFPHC EFSHC EFBSHC	EF * alloy, super heating, water quenching EF alloy + 30 ppm P, super heat, water quenching EF alloy + 195 ppm Sr, super heat, water quenching EF alloy + 195 ppm Sr + 500 ppm Be, super heat, water quenching

* EF alloy = E0 with 1.2%Fe total.

Table 3. Chemical compositions of selected alloys for tensile testing.

Alloy Codes	Composition
E	E0 + 0.35% Mg
E1	E + 0.5%Be
E2	E + 0.0030%P
E3	E, 0.8%Fe total
E4	E, 1.2%Fe total
E5	E, 1.52%Fe total
E6	E5 + 30 ppm P
E7	E5 + 0.05%Be
E8	E + 195 ppm Sr
E9	E + 380 ppm Sr
E10	E + 195 ppm Sr + 30ppm P

Table 3. Cont.

Alloy Codes	Composition
E11	E + 380 ppm Sr + 30ppm P
E12	E5 + 195ppm Sr
E13	E5 + 195 ppm Sr + 30ppm P
E14	E5 + 380 ppm Sr + 30ppm P
E15	E5 + 380 ppm Sr + 0.05%Be
E16	E5-superheated
E17	E12-superheated
E18	E14-superheated
E19	E6-superheated
E20	E13-superheated
E21	E15-superheated

The mold used was a Stahl permanent mold type ASTM B-108 [32]. Figure 1. This mold is symmetrical and allows two tensile test bars to be produced per casting. The interior of the mold is covered with two different coatings: one for the central part of the tensile bars and the other for the rest of the mold. The coating of the central part is graphite-based to allow rapid solidification, while the coating that covers the rest of the mold is made of vermiculite. The mold was preheated at 450 °C prior to casting in an electrical furnace. In order to minimize its formation, the molten metal was poured into the mold through a 20 ppi ceramic filter placed on the top of the sprue using a special set-up, as shown in Figure 1a,b. Figure 2 depicts the geometry of the standard tensile test bar obtained from the ASTM B-108 mold.

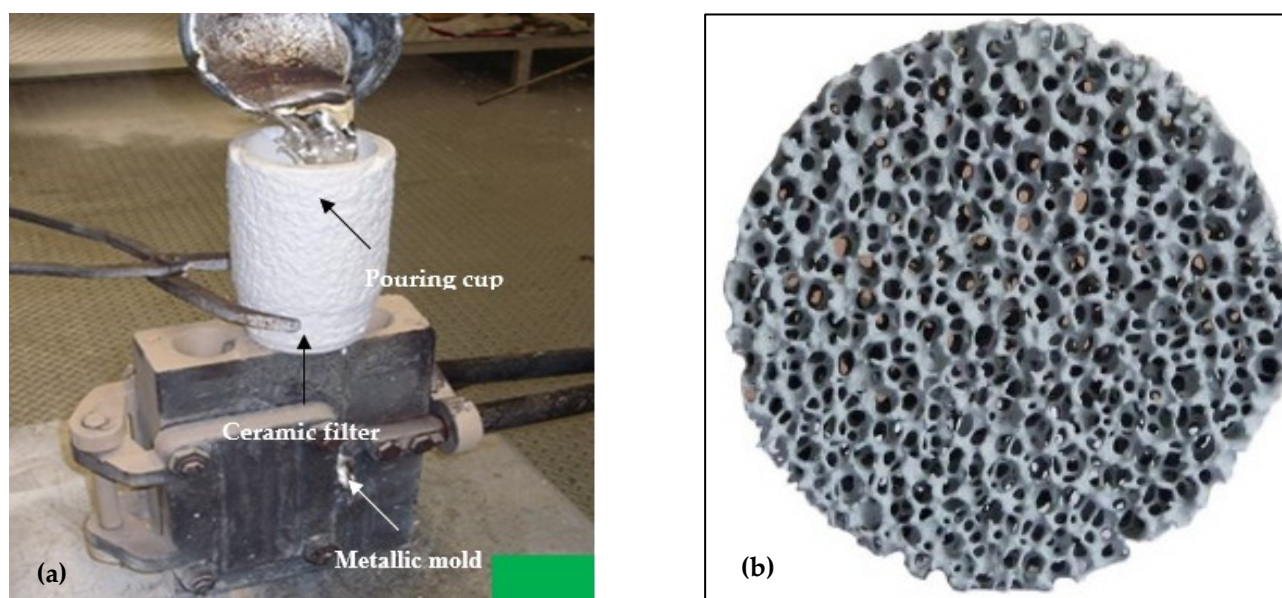


Figure 1. (a) Setup used for preparing the tensile test bars. (b) A ceramic 20ppi filter is placed at the bottom of the pouring cup, which is made of refractory material. The pouring cup is placed tightly on the top of the sprue of the metallic mold.

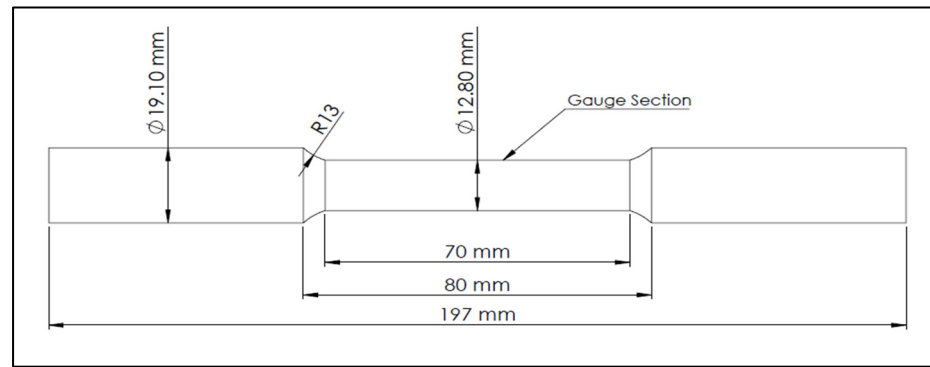


Figure 2. Geometry of the standard tensile test bar obtained from ASTM B-108 permanent mold.

In the setting of solutionizing treatment, the aforementioned furnace was pre-programmed according to a cycle such that, for each batch of test specimens, the temperature increased from room temperature to 495 °C in a period of 2 h. The tensile bars were put in at room temperature and ramped to 495 °C. The solution temperature of 495 °C was then maintained for a period of 8 h. Once the solution treatment was completed, the specimens were quenched from the temperature of 495 °C to room temperature. The setup for conducting the water quenching consists of a tank of water, which has a temperature that is close to 60 °C, and into which the test pieces taken out of the furnace were immersed.

Once cooling by quenching was complete, the test pieces were reheated in the furnace according to one of the five chosen artificial aging treatments (temperatures and times pre-programmed using the same programmable furnace). These methods of artificial aging consisted of taking turns to bring the temperature of a batch of test pieces from room temperature to 155 °C in half an hour. The artificial aging temperature was maintained for a period of 5 h. Cooling, at the end of artificial aging, was then conducted in ambient air. Subsequently, tensile tests were conducted on the test bars of selected alloys, where the as-cast bars were solution heat-treated and then artificially aged as per the five selected aging treatments.

The tensile specimens were tested using an MTS Servohydraulic Mechanical Testing machine (MTS Systems, Eden Prairie, MN, USA) at a strain rate of 4×10^{-4} /s. The data were collected by a data acquisition system connected to the machine. Conversion software processes this data to transform elongation into strain and force into stress. The software numerically determines the elastic limit (YS), the ultimate tensile strength (UTS), and the %Elongation to failure. The latter was obtained using a 2-inch extensometer attached to the gauge length of the bar (also supplied by MTS Systems).

Thermal analyses were conducted on the ingots of the alloys studied. Each experiment involved melting the alloy sample at ~725 °C and pouring the liquid metal into a graphite mold preheated at 600 °C. A type-K (chromel-alumel) thermocouple was installed through a hole at the bottom of the graphite mold, reaching the center of the mold and connecting to a computer using the installed software that recorded the temperature-time data. The solidification curve and its first derivative could then be plotted upon pouring the molten metal into the preheated mold. The solidification curves describe the evolution of the solidification temperature of the alloys studied as a function of time, and the first derivative curves describe the stages of formation of the various phases present in these alloys.

The observations of the microstructure were conducted with an Olympus BH2UMA optical microscope (Supplier: Evident Canada Inc., Québec, Quebec G1P, Canada) as well as with a JEOL JXA-8900L WD/ED (JEOL USA Inc., Peabody, MA, USA) electron microprobe that was operated at a voltage of 20 KV and a current of 30 Nano amperes. The latter made

it possible with the backscattered electron imaging mode to obtain high magnification images of the microstructure while using energy dispersive X-rays (EDX) and wavelength dispersion spectroscopy (WDS) to analyze the chemical compositions of different phases.

3. Results and Discussion

3.1. Characteristics of β -Al₅FeSi Platelets

Table 4 documents the combined effects of both the solidification rate and alloy composition on the characteristics of β -Al₅FeSi platelets, including average platelet length, average platelet thickness, platelet density, and average total surface area/cm². Increasing the solidification rate in terms of a DAS of about 80–90 μm obtained with the preheated graphite mold casting to 15–20 μm when using the permanent metallic mold reduced the average platelet length by about 82%. Further reduction to about 98% was achieved when the molten metal was poured directly into water (water quench in Table 4) in the form of droplets (the solidified droplets provided a DAS of about 3.5 μm).

Table 4. Effect of mold type on post-dendritic β -Al₅FeSi platelet characteristics.

Mold Type/DAS *	Alloy Code	Av. Length (μm)	Av. Thickness (μm)	Density (#/cm ²)	Av. Surface Area ($\mu\text{m}^2/\text{cm}^2$)
Graphite mold DAS 80–90 μm	EFHG	389 \pm 6	12.3	1.1 \times 10 ³	1.1 \times 10 ⁷
	EFPHG	174 \pm 3	10.4	5.2 \times 10 ³	6.0 \times 10 ⁷
	EFSHG	124 \pm 4	3.4	6.2 \times 10 ³	8.7 \times 10 ⁶
	EFBSHG	52 \pm 3	3.0	2.9 \times 10 ⁴	9.4 \times 10 ⁶
	EFHM	54 \pm 2	2.1	3.9 \times 10 ⁴	3.6 \times 10 ⁶
Metallic mold DAS 15–20 μm	EFPHM	63 \pm 3	2.4	3.1 \times 10 ⁴	5.7 \times 10 ⁶
	EFSHM	17 \pm 7	1.5	4.5 \times 10 ⁵	2.5 \times 10 ⁶
	EFBSHM	8 \pm 5	0.9	5.9 \times 10 ⁴	7.5 \times 10 ⁵
	EFTHM	7 \pm 3	0.8	3.9 \times 10 ⁵	3.5 \times 10 ⁵
	EFZHM	13 \pm 4	1.4	3.6 \times 10 ⁵	1.1 \times 10 ⁵
Water quench (solid droplet) DAS = 3–5 μm	EFTZHM	5 \pm 2	0.8	2.7 \times 10 ⁵	2.8 \times 10 ⁵
	EFHC	7 \pm 3	0.2	4.5 \times 10 ³	6.3 \times 10 ³
	EFPHC	9 \pm 5	0.2	1.2 \times 10 ⁴	2.2 \times 10 ⁴
	EFSHC	Nil	Nil	Nil	Nil
	EFBSHC	Nil	Nil	Nil	Nil

* DAS: dendrite arm spacing.

Modification with 195 ppm Sr proved to be effective in further reducing the β -platelet average length by about 70% for the hot graphite mold, whereas a combined high solidification rate (metallic mold) and Sr treatment resulted in bringing down the platelet length by about 96%.

Apparently, the addition of Be together with Sr is capable of reducing the β -platelet length by 87% and by 96% for the hot graphite mold and metallic mold, respectively. The addition of Ti or Zn in place of Be resulted in the same effect. It is evident from the platelet density that all melt treatments caused marked fragmentation of the initial length of the β -platelets. Another point that may be considered is that P, or more precisely, ALP particles, may act as nuclei for the precipitation of the platelets. However, this process is associated with a high fluctuation in the measurements (standard deviation). It should be kept in mind that all these alloys were superheated at 950 $^{\circ}\text{C}$ prior to casting from 750 $^{\circ}\text{C}$.

Grain refining using the Al-5%Ti-1%B master alloy was recommended by several authors as an effective method for improving the alloy strength [33–37]. Table 5 highlights the role of grain refiner on the fragmentation of β -platelets in the present study. As may be seen, the introduction of TiB₂ to the molten metal followed by superheating treatment resulted in a significant decrease in the length of the platelets, and the reaction was more effective when the alloy was grain refined and Sr-modified. In addition, the difference in platelet length between superheated alloys and those poured directly from 750 $^{\circ}\text{C}$ is about

$\pm 20\%$ [38,39]. Figure 3 depicts the precipitation of an Fe-rich phase on the AIP particles in the EFPHT alloy sample.

Table 5. Effect of solidification rate and grain refiner on the characteristics of β -platelet-metallic mold.

Superheating Temperature, (°C)	Alloy Code	Av. Length (μm)	Av. Thickness (μm)	Density ($\#/\text{cm}^2$)	Av. Total Surface Area ($\mu\text{m}^2/\text{cm}^2$)
950 °C	EFHM	54 ± 18	2.1	3.9×10^4	3.6×10^6
950 °C	EFHT	20 ± 1	1.5	2.0×10^5	6.0×10^6
	EFPHT	91 ± 7	2.1	2.1×10^4	4.0×10^6
	EFSHT	20 ± 2	1.6	2.1×10^5	7.0×10^6
	EFPSHT	17 ± 9	1.1	2.0×10^5	3.7×10^6
	EFBSHT	8 ± 2	0.7	4.6×10^5	3.3×10^6
750 °C	EFT	25 ± 5	0.8	2.0×10^5	4.0×10^6
	EFPT	32 ± 2	1.7	6.3×10^4	3.4×10^6
	EFST	22 ± 1	0.8	2.1×10^5	3.7×10^6
	EFPST	22 ± 1	1.1	1.2×10^5	4.0×10^6
	EFBST	12 ± 8	0.7	2.4×10^5	1.1×10^6

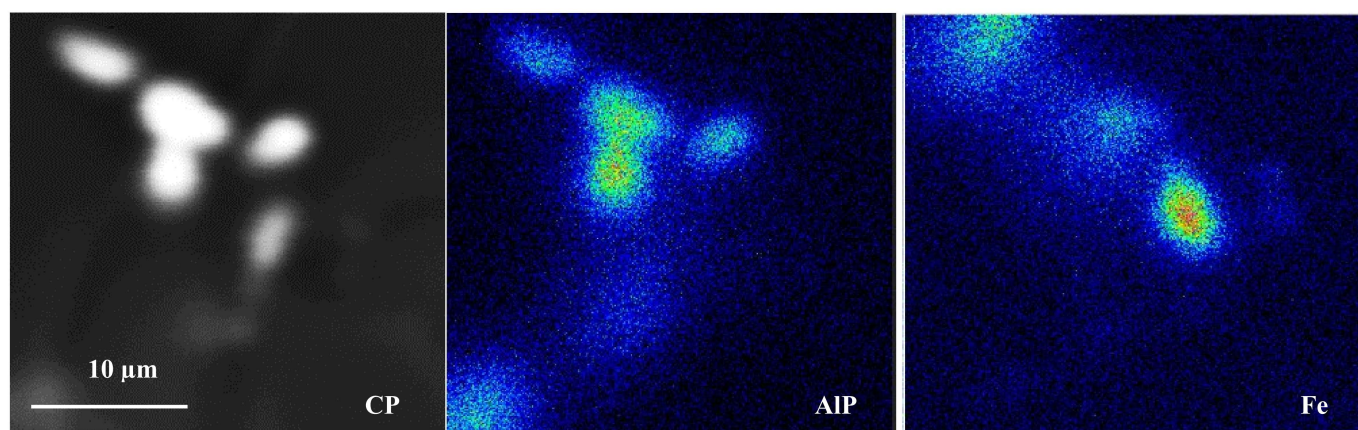


Figure 3. Precipitation of Fe compounds on the AIP particles in EFPHT alloy.

3.2. Microstructural Characterization

Figure 4 illustrates the solidification curves of 413.0 alloy in the non-modified (Figure 4a) and Sr-modified (Figure 4b) conditions, respectively. Based on Figure 4, the melting point of the base alloy is about 570 °C. Modification with Sr has no effect on either the melting temperature or the solidification time of ~ 550 – 600 s. Table 6 summarizes the details of the solidification curves presented in Figure 4 in terms of the different parameters involved. In the present section, the EF alloy contains about 1.2% Fe, which is close to the Fe content in high-pressure die-casting alloys such as the B380.1 alloy [40–42]. As seen in Table 4, with the increase in solidification rate, the average length of the β -platelets decreased from about 400 μm to ~ 7 μm , with the decrease in the DAS from 90 μm to ~ 3 μm , as shown in Figure 5.

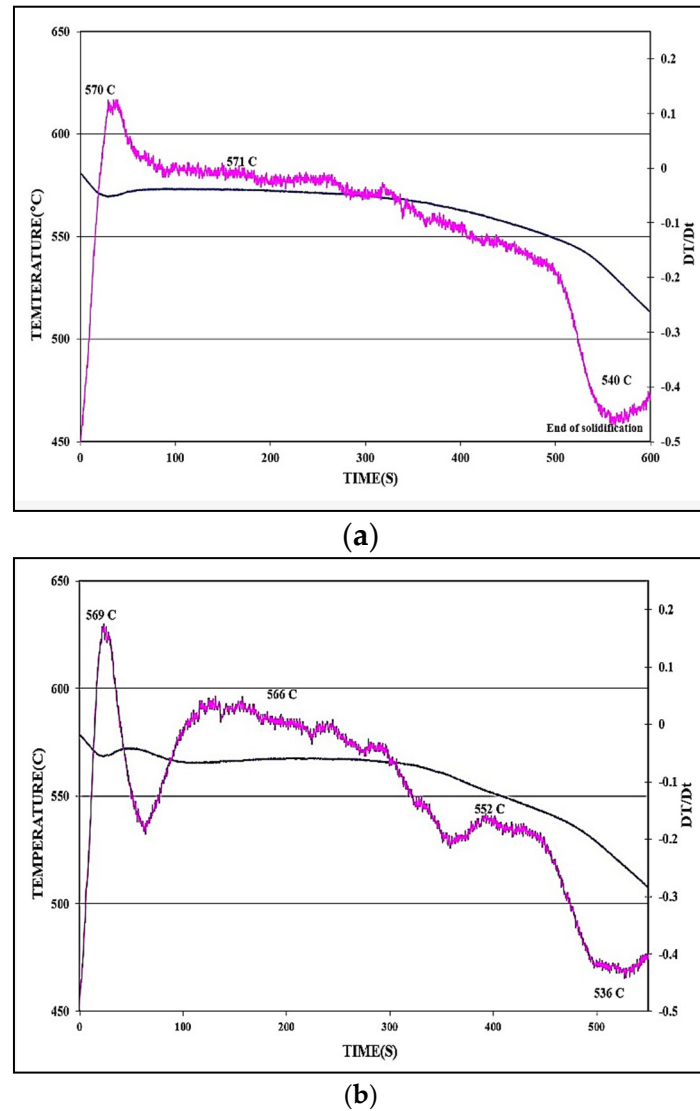


Figure 4. Temperature-time solidification curves and their first derivatives (in fuschia color) for: (a) non-modified, and (b) Sr-modified 413 alloy. Alloys were cast in the 600 °C preheated graphite mold.

Table 6. The effect of addition of Sr on the eutectic undercooling of 413 alloy, as seen in Figure 4.

Alloy	Undercooling Parameters Related to the Al-Si Eutectic Reaction					
	Te1 (°C)	Te2 (°C)	ΔT_e (°C)	te1 (s)	te2 (s)	Δt_e (s)
413 (Figure 4a)	570.1	571.3	1.4	124.4	233.6	132.2
431 + Sr (Figure 4b)	565.6	568.3	2.7	104.4	213.2	88.8

Pouring liquid metal from a temperature as high as 1050 °C produced a significant reduction in the length of the β -platelets to ~40 μm from about 250 μm for samples poured directly from 750 °C, due to enhanced rates of β -phase decomposition from Al_5FeSi to Al_6Fe [42], coupled with dissolution in the liquid metal, as seen in Figure 6. However, the application of such high temperatures will not allow for degassing using the graphite impeller, as described in the experimental procedure section.

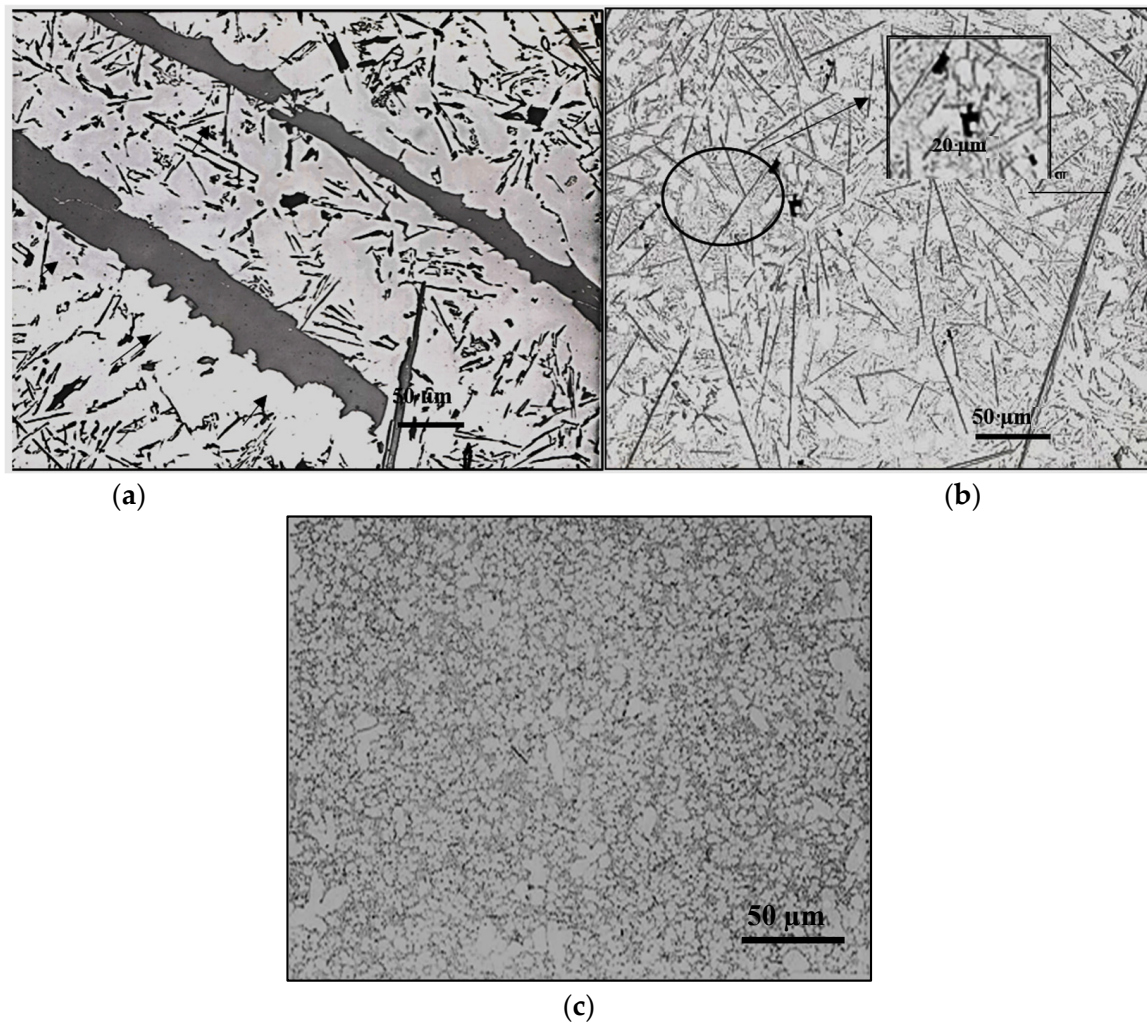


Figure 5. Effect of solidification rate on the size and distribution of β -platelets in: (a) hot graphite mold sample (DAS $\sim 90 \mu\text{m}$); black arrows show necking prior to fragmentation; (b) metallic mold sample (DAS $\sim 20 \mu\text{m}$); (c) solidified droplet from direct quench in cold water (DAS $\sim 3 \mu\text{m}$). Inset in (b) shows precipitation of microporosity on the surfaces of β -platelets.

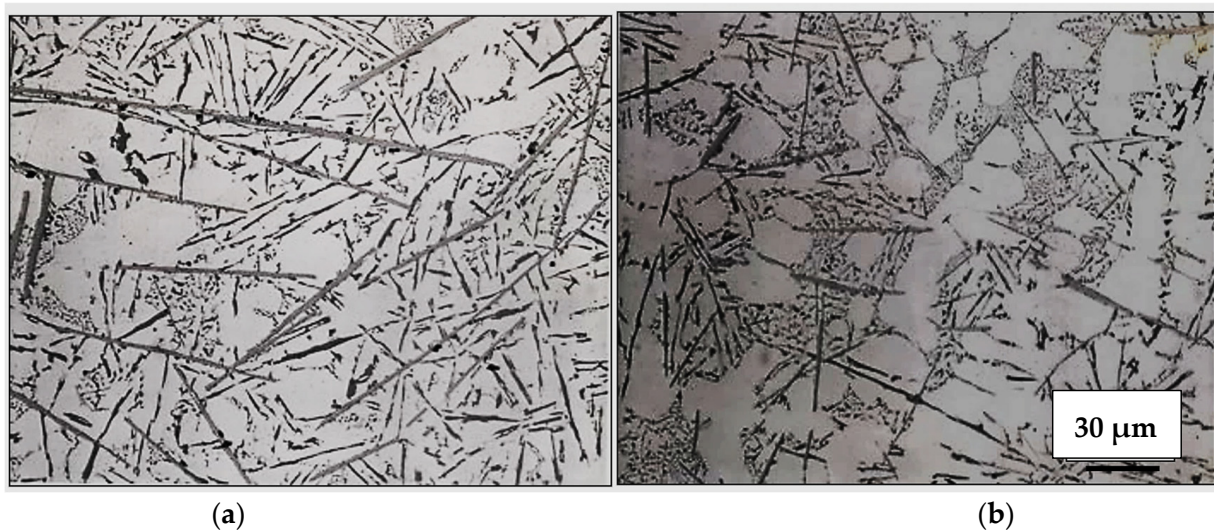


Figure 6. Effect of direct pouring temperature on the size and distribution of β -platelets: (a) $750 \text{ }^\circ\text{C}$, (b) $1050 \text{ }^\circ\text{C}$. Samples were cast in the metallic mold.

According to the Ellingham diagram [43], at such high temperatures, Al, Mg, and Sr have a high affinity to react with oxygen, forming different oxides i.e., Al_2O_3 , MgO, and SrO, as depicted in the microstructure shown in Figure 7, which reveals massive aluminum oxide films (black arrow) and SrO (white arrow). These oxides are suitable sites for precipitation of β -platelets and would significantly deteriorate the alloy strength [44–46]. In contrast, for samples cast from 750°C , Figure 8 exhibits scattered SrO spots rather than patches as seen in Figure 7. Although Sr was added to the molten metal just before pouring, it is impossible to stop the formation of SrO. Another problem encountered with pouring directly from 1050°C is excessive fluidity of the liquid metal, leading to leaking of the metal out of the mold, resulting in an incomplete casting, as shown in Figure 8a, compared to the casting with molten metal poured from 750°C , as depicted in Figure 8b. Figure 8c depicts the precipitation of SrO oxide in the form of fine dispersed particles/patches when the molten metal was poured from 750°C and passed through a ceramic filter prior to entering the mold, as was shown in Figure 1.

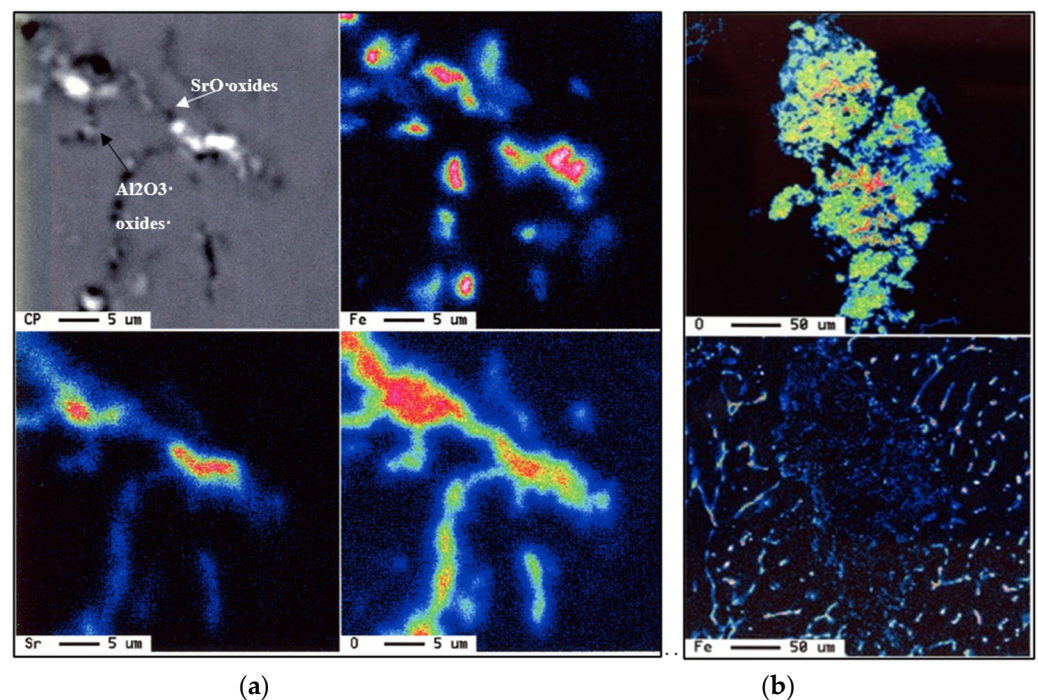


Figure 7. (a) Oxide films associated with samples poured directly from 1050°C , showing precipitation of Fe intermetallic on the edges of the oxide film, (b) precipitation of Fe-containing phase particles on the edges of an oxide film.

The combined effect of adding both Sr and Be, coupled with the solidification rate on the size and distribution of the β -platelets, is presented in the optical micrographs of Figure 9. As can be observed, the use of Be has enhanced the fragmentation and dissolution process of the β -platelets, leading to a significant reduction in their length from about $150\ \mu\text{m}$ (Figure 9a) to about $10\text{--}15\ \mu\text{m}$ (Figure 9b). As mentioned previously in the introduction section, Fe reacts with Be, forming a complex compound, i.e., the $\text{BeSiFe}_2\text{Al}_8$ phase, which would lower, to some extent, the concentration of free Fe. Hence, the amount of active Fe to form the β phase would be less than the added Fe.

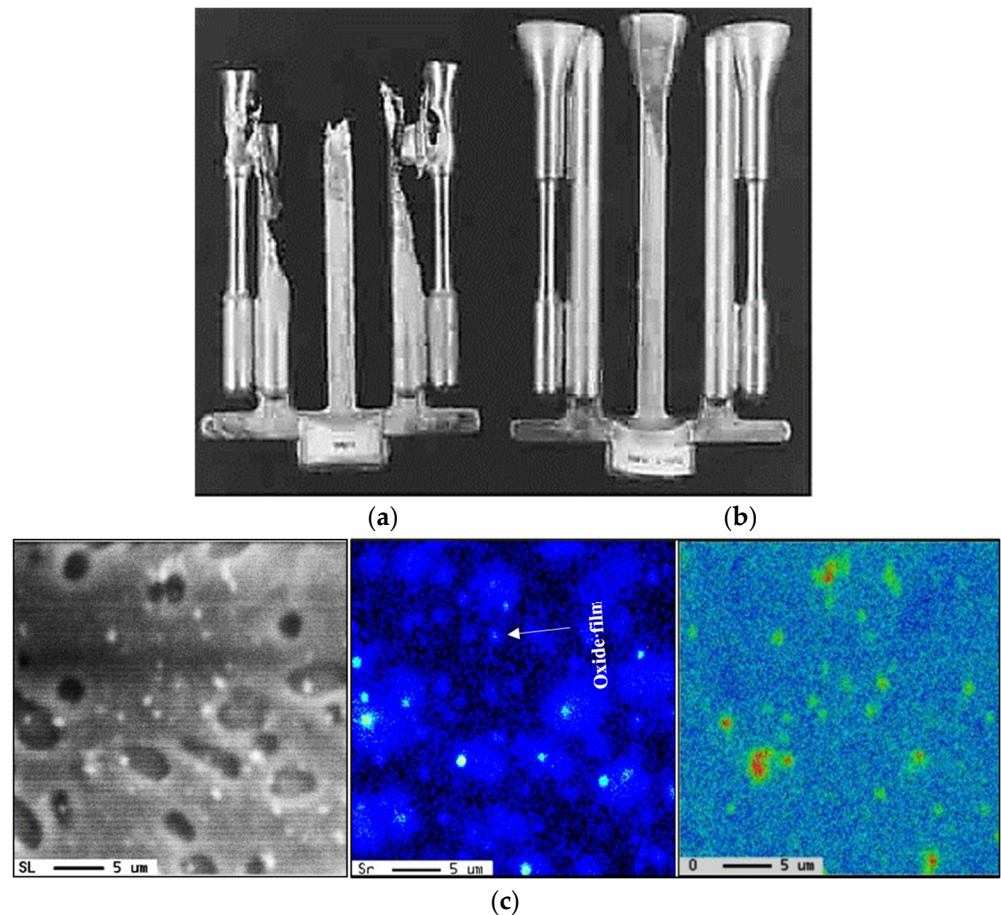


Figure 8. (a) Pouring temperature about 1050 °C—incomplete casting, (b) pouring temperature 750 °C—complete casting, (c) size and distribution of SrO in samples poured from 750 °C following degassing for 30 min using pure dry argon gas.

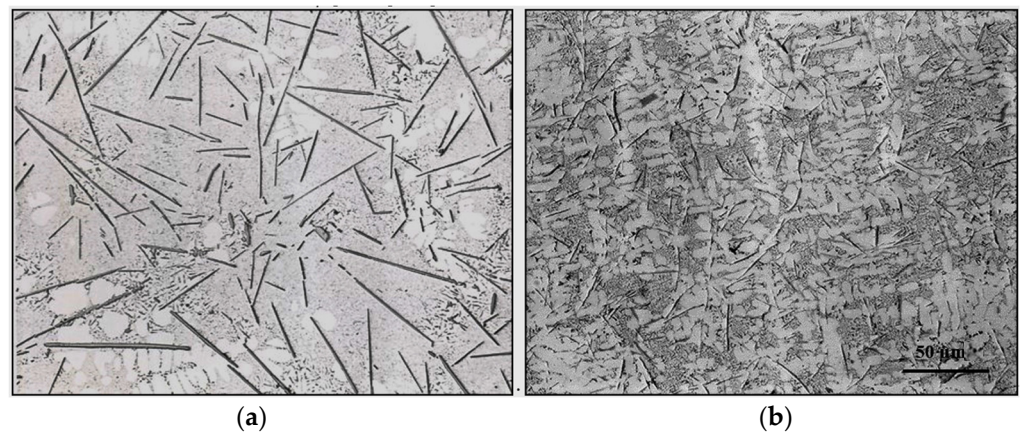


Figure 9. Combined effects of solidification rate, Sr modification, and addition of Be on the size and distribution of β -platelets: (a) graphite mold, (b) metallic mold. Both melts were superheated at 950 °C.

Figure 10 illustrates the role of added Ti (in the form of TiB_2 , Figure 10a), or 1% Zn (Figure 10b). In Figure 10, the same alloys shown in Figure 9 are observed accelerating the rates of fragmentation of the β -platelets. It is evident that none of these additions brought about marked changes above those displayed in Figure 10b. In other words, the main role of using Ti or Zn is grain refining or accelerating the hardening rate, respectively. In other words, the main role of using Ti or Zn is grain refining or accelerating the hardening

rate, respectively. Another aspect to be highlighted is the spheroidization of the β -platelets when applying the water quenching method, as depicted in Figure 10c. Figure 11 illustrates the role of La as an active site for β -phase precipitation.

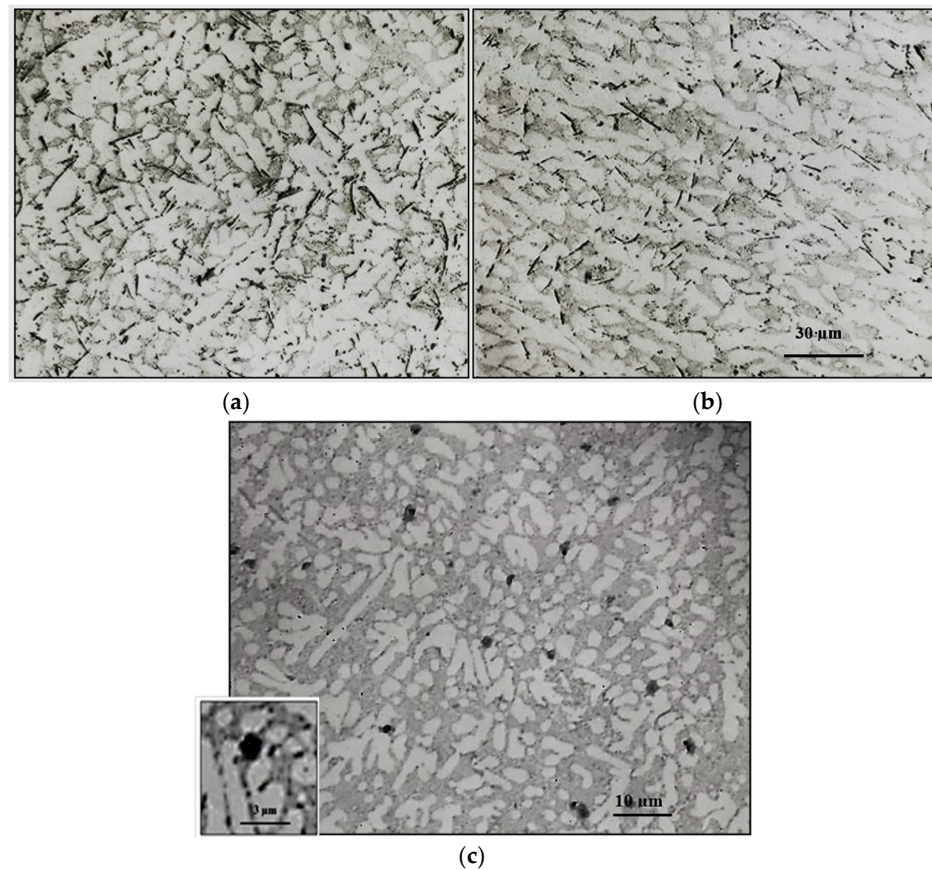


Figure 10. Effect of added TiB_2 or Zn to the Sr +Be-containing alloy on the size and distribution of β -platelets: (a) TiB_2 (0.2%Ti)—metallic mold sample, (b) 1%Zn—metallic mold sample, (c) Sr+Be-containing alloy—solidified droplet (water quenching method). All samples were superheated at 950 °C and poured from 750 °C.

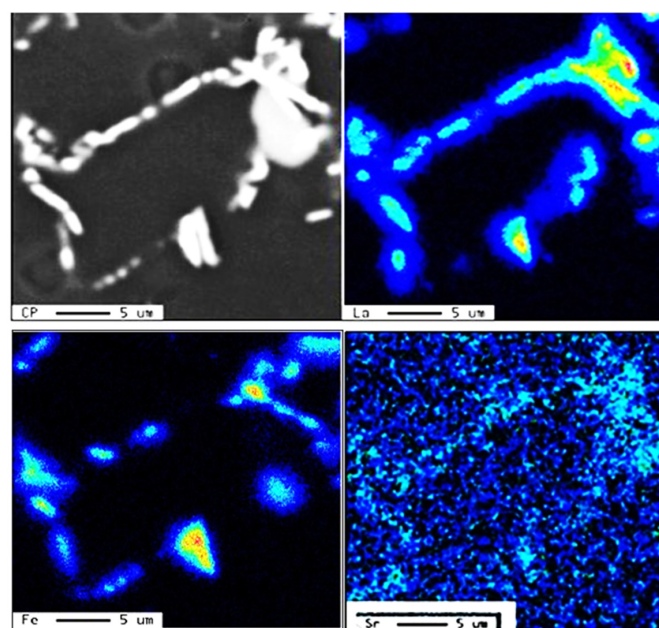


Figure 11. Precipitation of β -phase particles in La-containing Sr-modified 413 alloy (metallic mold).

3.3. Tensile Properties

Figure 12 depicts the effects of the various alloying elements on the tensile properties of the selected alloys (see Table 3) in the T6 condition. The contribution of these additives to the base alloy E is summarized in Table 7 (details for the calculation of ΔP are presented in Appendix A). As highlighted in Figure 12, the addition of Be or P to the E (413.0 + 0.35%Mg) alloy resulted in a slight increase in both UTS and YS, with decreases in the alloy ductility (Series #1) due to partial conversion of the β -platelets into the compacted BeSiFe₂Al₈ phase, or fragmentation of the platelets, resulting in the formation of the Al₆Fe phase.

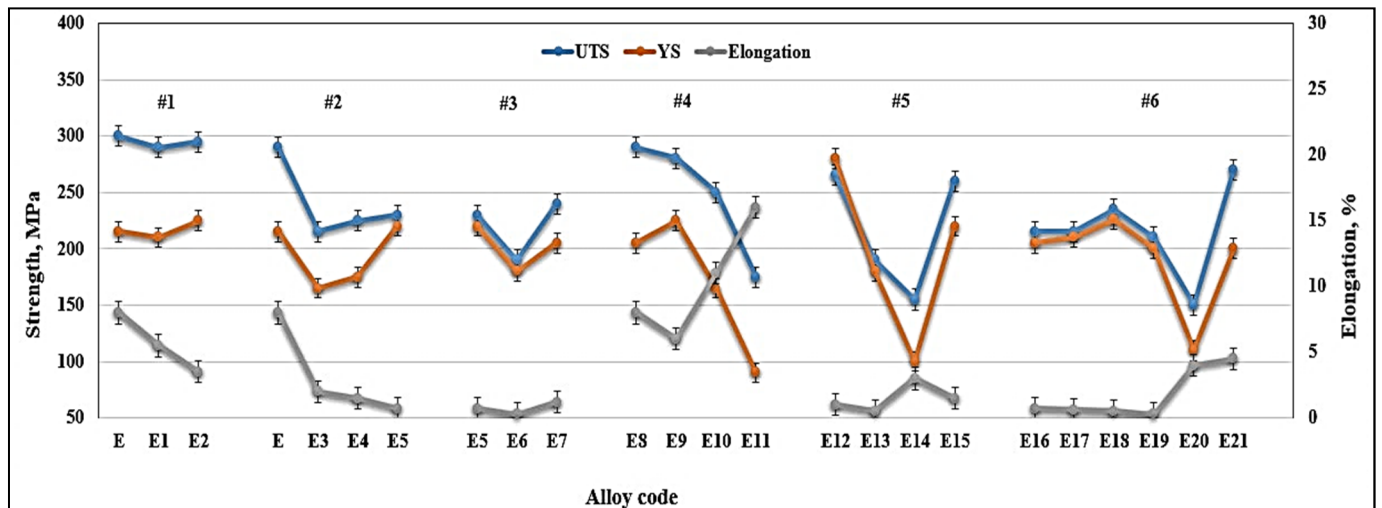


Figure 12. Variation in the alloy tensile parameters as a function of alloy composition.

Table 7. Values of ΔP (P = Property) for the six series of alloys selected for tensile testing.

Alloy	ΔP –UTS (MPa)	ΔP –YS (MPa)	ΔP –%EL
Series #1			
E	0	0	0
E1	–10	–5	–2.5
E2	–5	10	–4.5
Series #2			
E	–10	0	0
E3	–85	–40	–6
E4	–80	–35	–6.5
E5	–70	5	–7.3
Series #3			
E5	–70	5	–7.3
E6	–110	–35	–7.7
E7	–60	–10	–6.8
Series #4			
E8	–10	–10	0
E9	–20	10	–2
E10	–50	–50	3
E11	–125	–125	8
Series #5			
E12	–35	65	–7
E13	–110	–35	–7.5

Table 7. Cont.

Alloy	ΔP –UTS (MPa)	ΔP –YS (MPa)	ΔP –%EL
E14	–145	–115	–5
E15	–40	5	–6.5
Series #6			
E16	–85	–10	–7.3
E17	–85	–5	–7.4
E18	–65	11	–7.5
E19	–90	–15	–7.7
E20	–150	–105	–4
E21	–30	–15	–3.5

Series #2 represents the influence of increasing the concentration of Fe to 1.8% total. Increasing the Fe content from 0.4% in E0 alloy to 0.8% caused a drop in the UTS, YS, and %EL levels by about 30 MPa, 83 MPa, and 5.5%, respectively, followed by a marginal increase in these parameters, with a further increase in Fe added to ~1.8% in total. This may be attributed to the hardening effect of the fragments of β -platelets, as shown in Figure 5b, similar to the behavior of metal matrix composites [47–52].

The addition of P to the alloy melt results in the precipitation of a large number of AlP particles (see Figure 13). The resulting increase in density of the β -platelets (see Table 7) will eventually ruin the alloy mechanical properties, particularly in alloys with a high Fe content, such as the E6 alloy, causing a significant drop in the values of UTS, YS, and %EL by 205 MPa, 110MPa, and about 6%, respectively. Although the addition of Be (E7 alloy) revealed a tendency to improve the alloy tensile parameters, the values of UTS and YS were 50–100 MPa below the levels obtained for the E alloy.

Series #4 and #5 highlight the beneficial effect of modifying the alloys with Sr in accelerating the fragmentation rates of the β -platelets, as shown in Figure 10b, which, in turn, would contribute to the alloy strength. The effect of strontium as a modifier is attenuated by the presence of phosphorus, which reacts with it. Thus, alloys containing high concentrations of phosphorus require greater amounts of strontium to produce an acceptable microstructure.

Large primary silicon crystals adversely affect the mechanical properties of Al-Si alloys [53,54] e.g., as in the case of the E11 alloy. Figure 13a illustrates the precipitation of primary Si particles on AlP particles (inset micrograph). In this case, the precipitation of primary Si is followed by the eutectic reaction. However, in the E9 alloy, containing 320 ppm Sr, crystals of $\text{Al}_2\text{Si}_2\text{Sr}$ phase particles (grey color) precipitate all over the matrix, as seen in Figure 13b. Considering the high hardness of Si (7 Mohs), these particles would contribute to the alloy strength [55], counteracting the negative effect of 1.8%Fe in the E15 alloy along with the presence of Be. Nevertheless, the degradation effect of P could not be overcome by high Sr addition, bringing the alloy tensile parameters far below those offered by the base E alloy (i.e., ΔP values of –150 MPa (UTS), –120 MPa (YS), and –22%EL, taking the base E alloy ($\Delta P = 0$) as the reference line). According to Gao et al. [56] and Barrirero et al. [57], the treatment of Al-Si alloys with Sr and the formation of the $\text{Al}_2\text{Si}_2\text{Sr}$ phase would neutralize the nucleation of Si, reducing the frequency of their precipitation. The data presented in Tables 4 and 5 showing the effect of superheating and additives on the dimensions of β -platelets are plotted in Figure 14a. As can be seen, the addition of P results in the precipitation of massive β -platelets, causing major deterioration of the tensile properties. Although Be is toxic, careful use will counteract the negative effect of P. Figure 14b depicts the variation in the density of β -platelets as a function of types of additives and superheat. As can be observed, the behavior of particle density is opposite to

that noted for the average length and thickness parameters of the β -platelets displayed in Figure 14a.

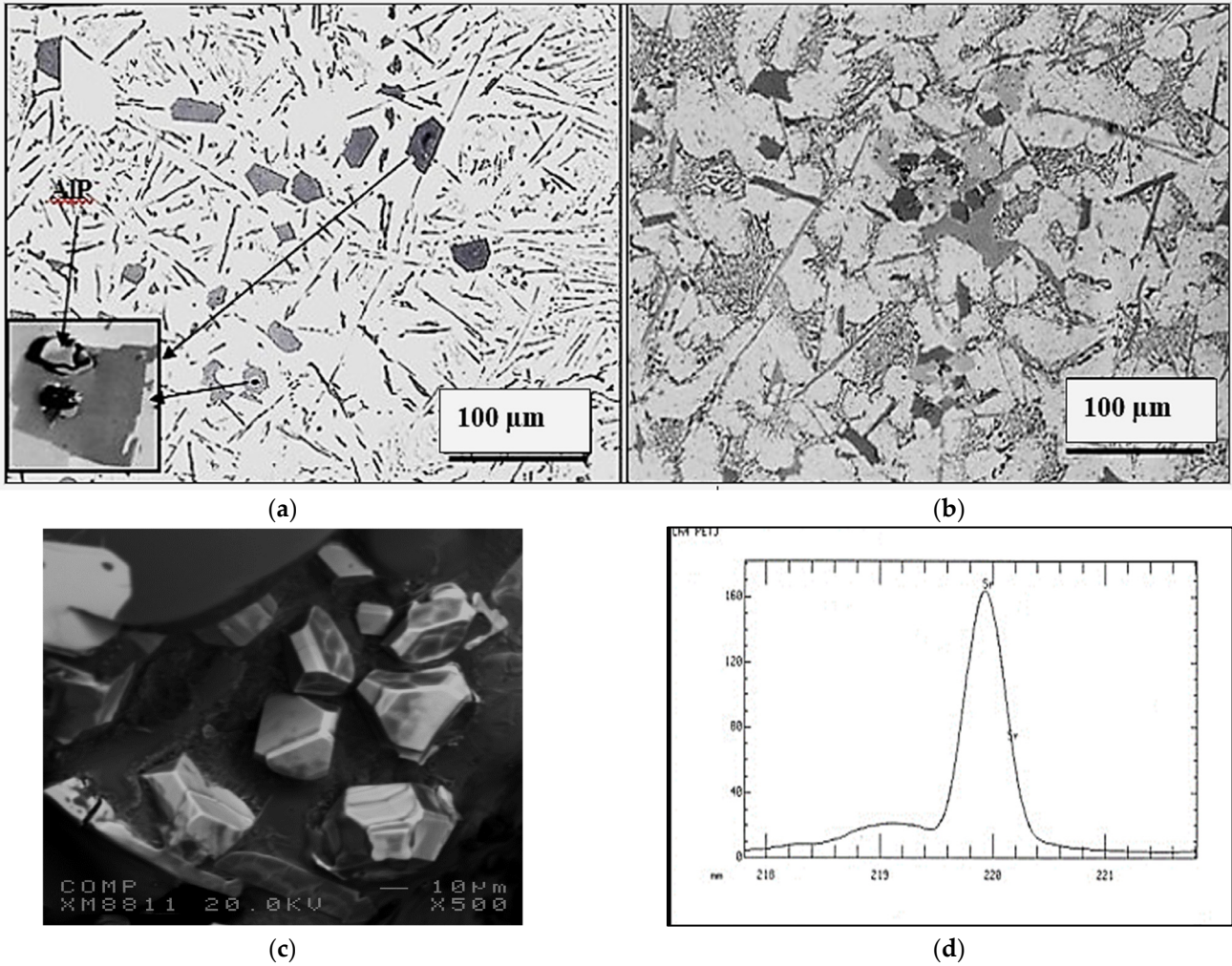


Figure 13. Effect of P addition on the precipitation of: (a) primary Si particles (non-modified alloys), (b) precipitation of Al_2Si_2Sr phase particles in Sr-modified alloys, (c) an example of 3D shape of Sr-containing precipitates, (d) scan through (c).

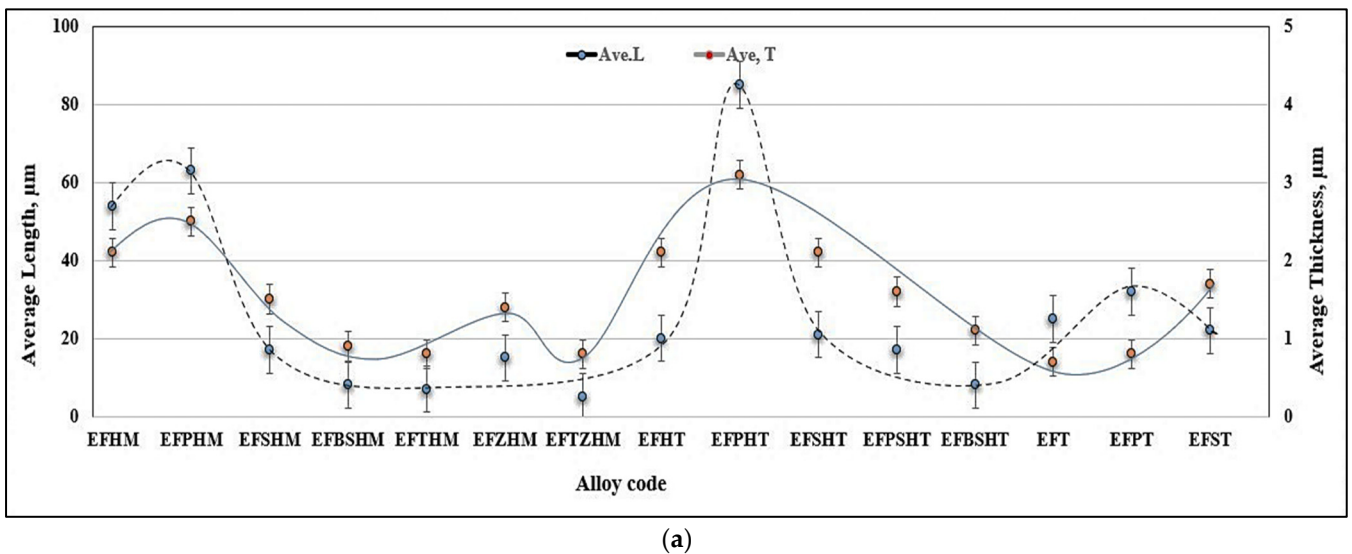
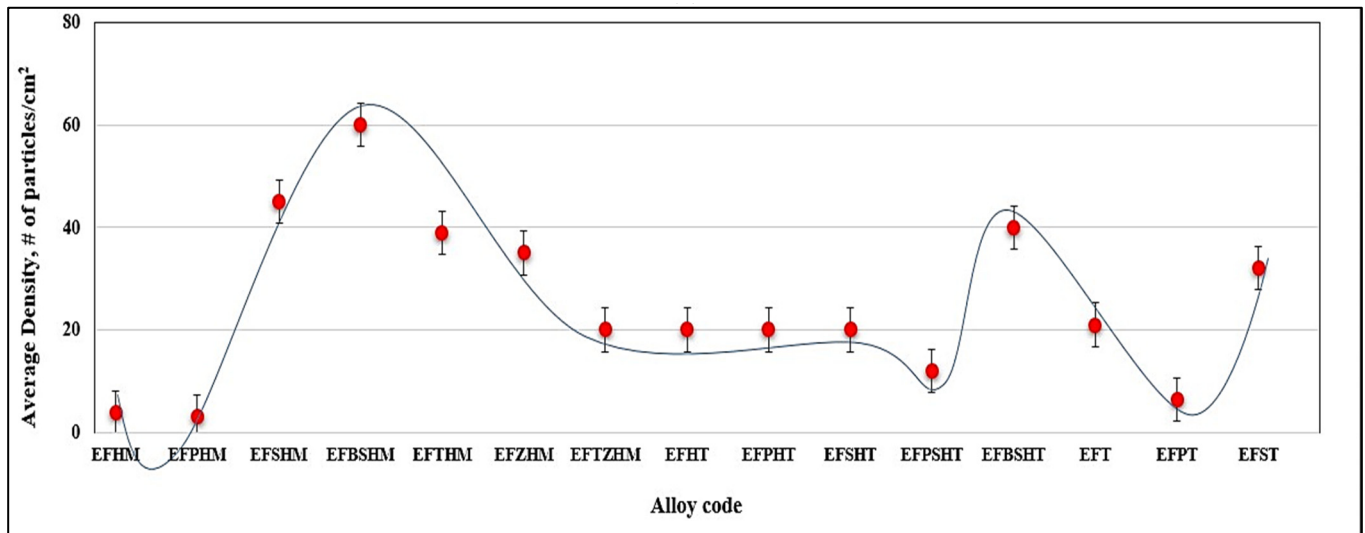


Figure 14. Cont.



(b)

Figure 14. (a) Effect of additives and superheating on the average length and average thickness of β -platelets—samples obtained from metallic mold castings; see Tables 4 and 5 for details. (b) Effect of additives and superheat on the density of β -platelets.

Another point to consider is the role of superheating. Series #6 shows that alloys E16 to E18 are characterized by their brittleness, with their ductility reaching about 0.5% (compared to 15% for alloy E), whereas alloy E19 revealed some recovery in ductility (about 5%). As in the other cases discussed above, the addition of 500 ppm Be proved to be very effective in counteracting the loss in the alloy tensile strength properties (ΔP values of -25 MPa (UTS), 10MPa (YS), and -17% EI). One of the main reasons for the observed decrease in alloy strength in high Fe-content ($\sim 1.8\%$) alloys is the porosity formation caused by the restriction of fluid motion to fill up the gap between the intercepting long β -platelets, as illustrated in Figure 15.

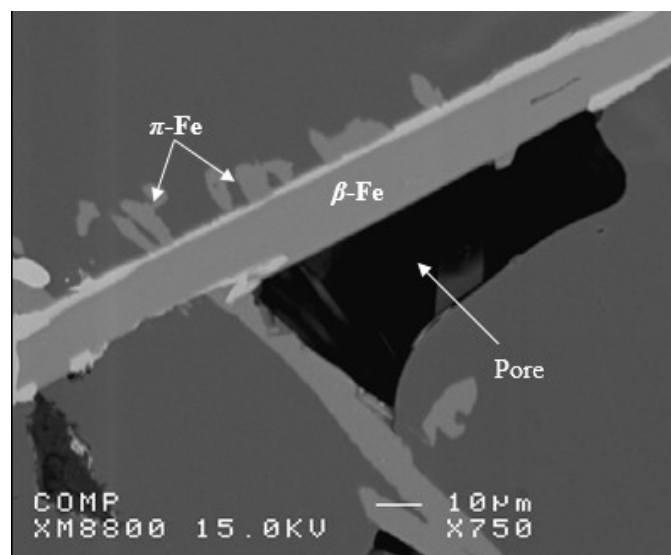


Figure 15. An example of reduction in the molten metal circulation by long intercepting β -platelets in 1.8%Fe-containing alloys solidified at 0.8 °C/s.

3.4. Alloy Quality: Interpretation of Tensile Properties Using the Quality Index

The quality of aluminum alloy castings may be defined using numerical values, which correlate with their mechanical properties. Drouzy et al. [58,59] first proposed these

numerical values in 1980 and termed them quality indices. These may be represented by the following equation:

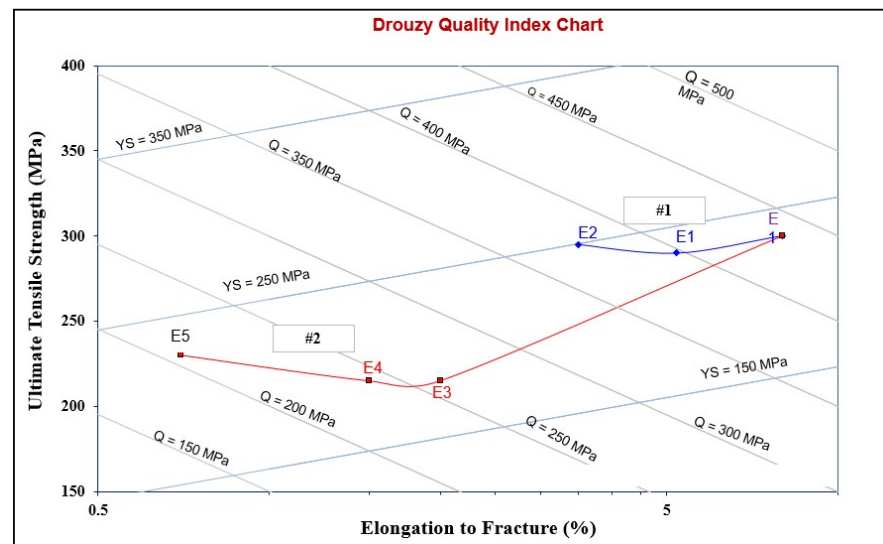
$$Q = \sigma_{uts} + d \log (E_f) \tag{1}$$

where Q is the quality index in MPa ; σ_{uts} refers to the ultimate tensile strength in MPa ; E_f refers to the percentage elongation to fracture; and d is a material constant equal to 150 MPa for Al-7Si-Mg alloys. The probable yield strength, $\sigma_{P(Y_S)}$, for the same alloy may be proposed as:

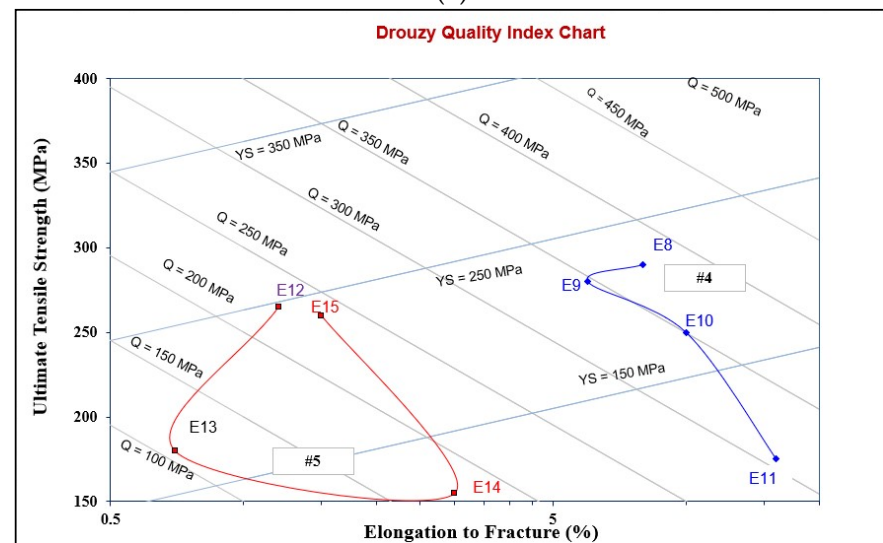
$$\sigma_{P(Y_S)} = a \sigma_{UTS} - b \log (E_f) + c \tag{2}$$

where the coefficients a , b , and c for Al-7Si-Mg alloys were determined as 1, 60, and -13 , respectively, with the constants b and c expressed in units of MPa .

Figure 16a presents the Quality Index chart as proposed by Drouzy et al. [58,59], showing the Q values for the Series #1 and Series #2 alloys. A significant drop in quality of the E alloy is noted once the Fe content is increased to 0.8% (from 430 MPa to about 250 MPa), whereas increasing the Fe concentration to 1.8% resulted in a marked decrease in the alloy ductility and, hence, its Q -value or quality (~ 200 MPa).



(a)



(b)

Figure 16. Cont.

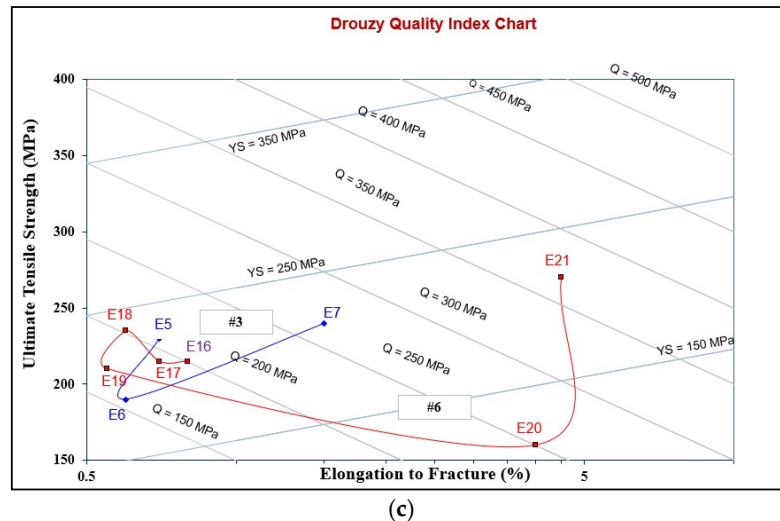


Figure 16. Quality values of the alloys used for tensile testing, tested in the T6-tempered condition: (a) Series #1 and #2, (b) Series #4 and #5, (c) Series #3 and #6.

Figure 16b illustrates the beneficial effect of modification with the right amount of Sr, as in the case of alloy E8, which achieves a Q-value of about 380 MPa compared to 430 MPa for the non-modified E alloy. The difference may be brought about by the porosity caused by the formation of SrO, as exemplified in Figure 17. Over-modification with 320 ppm Sr, coupled with the precipitation of $\text{Al}_2\text{Si}_2\text{Sr}$ phase particles (shown in Figure 13b), resulted in a decrease of the Q-value of the E8 alloy by about 30 MPa for the E9 alloy.

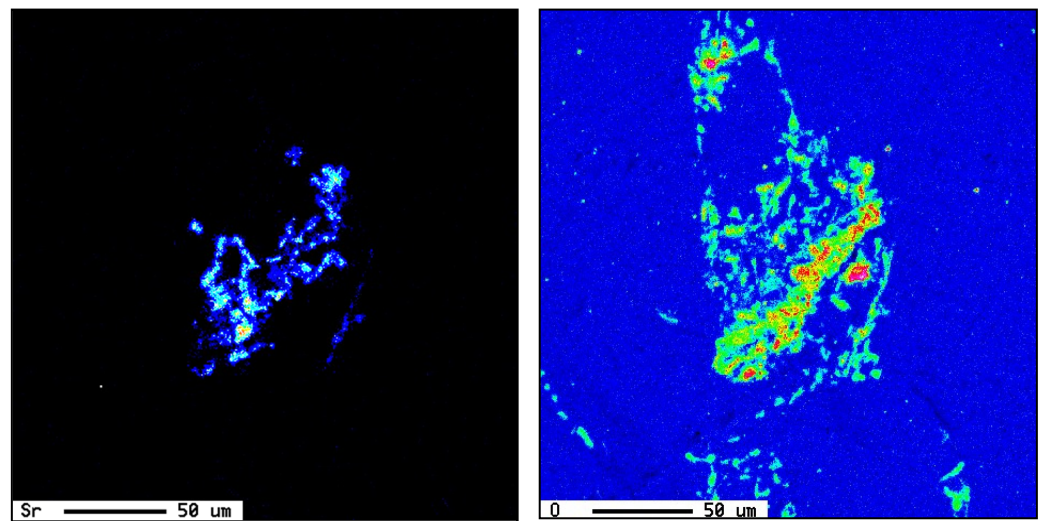


Figure 17. Formation of SrO in E8 alloy.

The use of 30 ppm P and its ability in increasing the volume fraction of primary Si and nucleation of $\text{Al}_2\text{Si}_2\text{Sr}$ particles led to a reduction in the UTS level. However, there was no marked effect on the Q-values due to the improvement in the alloy ductility.

When increasing the Fe content to 1.8%, Sr addition increased the Q-index to about 230 MPa, which is very close to that achieved by the E5 alloy and E15 alloy containing 500 ppm Be. The worst values were noted for the P-containing alloys, as seen in Figure 16b. Figure 16c reveals the effect of superheating on the Q-values of 1.8%Fe-containing alloys, showing a significant enhancement in the value of Q, reaching 370 MPa in the case of E21 alloy, compared to the untreated E5 alloy.

4. Conclusions

The current investigations were performed with a view to highlight the role of a number of metallurgical parameters on the tensile properties and quality indices of high-strength eutectic Al-11.7%Si-0.35%Mg-based alloys. The studied variables are: iron level; solidification rate; Sr, Be, P, Ti, and Zn addition. Quality charts were used for selecting the optimum conditions to be applied in the industry to achieve high strength and optimum quality in Al-Si castings. From the results obtained, the following salient points may be listed:

1. Iron has a marked degradation impact on both the strength and the quality of the 413 based alloy castings due to the size and morphology of the β platelets. Tolerable Fe concentrations and methods of neutralization/fragmentations or dissolution have been discussed.
2. The addition of Sr plays a significant role in improving the strength of these alloys. The combined addition of Sr and Be enhances the alloy performance due to destabilization of the β -Al₅FeSi platelets, and their consequent fragmentation, in addition to a partial transformation of the Al₅FeSi platelets to the new BeSiFe₂Al₈ phase, which has a polygonal shape or Chinese script form.
3. Applying superheating at 950 °C would reduce the average β -platelet length by about 95%, which facilitates their dissolution thereafter during the solutionizing treatment. Also, over-modification with Sr results in the precipitation of Al₂Si₂Sr polygonal particles, causing reduction in the alloy strength.
4. The addition of P has a strong tendency to deteriorate the alloy tensile properties and quality indices caused by accelerating the precipitation of Fe-containing intermetallic and primary Si and Al₂Si₂Sr phase particles, reducing the alloy ductility to about 0.6% from an initial value of 15% for the base alloy.
5. The addition of Ti or Zn has no effect on Fe-phase precipitation or dimensions.
6. Increasing the solidification rate to about 50 °C/s would lead to complete dissolution of 1.8%Fe in the aluminum matrix.

Author Contributions: Methodology, E.S. and E.E.; Software, E.E.; Formal analysis, H.W.D.; Investigation, A.M.S. and V.S.; Resources, V.S.; Writing—original draft, A.M.S.; Writing—review & editing, F.H.S.; Project administration, F.H.S. All authors have read and agreed to the published version of the manuscript.

Funding: This research received no funding.

Institutional Review Board Statement: Not applicable.

Informed Consent Statement: Not applicable.

Data Availability Statement: The original contributions presented in the study are included in the article, further inquiries can be directed to the corresponding authors.

Conflicts of Interest: The authors declare no conflict of interest.

Appendix A

A comparison of the tensile properties of the selected alloys studied in this investigation, using various additives and amounts, was conducted using a system where a comparison was made in terms of the difference in properties obtained using the base alloy as the reference alloy.

This system consists of observing the difference between the properties of an alloy and those of the base alloy 413.0 (coded E alloy), denoted by ΔP , where P represents a

property (P = UTS, YS, and %EL in the present case). The ΔP values presented in Table 6 were obtained by taking the base E alloy ($\Delta P = 0$) as the reference line.

The ΔP values were calculated as follows:

$$UTS_x - UTS_i = \Delta UTS_x$$

In this formula, UTS_x represents the ultimate limit (UTS) of the alloy with one or more new elements added to the base alloy. UTS_i represents the ultimate limit of alloy I; and ΔUTS_x is the difference between the two, which will serve as a comparison tool. The same calculation was also applied for the elastic limit (YS) and for the percentage elongation (%EL). Accordingly, a result with a positive value indicates an increase in properties, while a negative value means there has been a decrease.

References

- Zykova, A.P.; Chumaevskiy, A.V. The Formation of Iron-Containing Intermetallic Phases in Al-12%Si Alloy by Using Tungsten Addition. *Met. Microstruct. Anal.* **2020**, *9*, 360–368. [[CrossRef](#)]
- Otani, L.B.; Soyama, J.; Zepon, G.; e Silva, A.C.; Kiminami, C.S.; Botta, W.J.; Bolfarini, C. Predicting the Formation of Intermetallic Phases in the Al-Si-Fe System with Mn Additions. *J. Phase Equilibria Diffus.* **2017**, *38*, 298–304. [[CrossRef](#)]
- Zhang, X.; Wang, D.; Zhou, Y.; Chong, X.; Li, X.; Zhang, H.; Nagaumi, H. Exploring crystal structures, stability and mechanical properties of Fe, Mn-containing intermetallics in Al-Si Alloy by experiments and first-principles calculations. *J. Alloys Compd.* **2021**, *876*, 160022. [[CrossRef](#)]
- Ferraro, S.; Timelli, G. Influence of sludge particles on the tensile properties of die-cast secondary aluminum alloys. *Met. Mater. Trans. B* **2015**, *46*, 1022–1034. [[CrossRef](#)]
- Zhang, X.; Wang, D.; Li, X.; Zhang, H.; Nagaumi, H. Understanding crystal structure and morphology evolution of Fe, Mn, Cr-containing phases in Al-Si cast alloy. *Intermetallics* **2021**, *131*, 107103. [[CrossRef](#)]
- Gao, T.; Hu, K.; Wang, L.; Zhang, B.; Liu, X. Morphological evolution and strengthening behavior of α -Al(Fe,Mn)Si in Al-6Si-2Fe-xMn alloys. *Results Phys.* **2017**, *7*, 1051–1054. [[CrossRef](#)]
- Dietrich, B.G.; Becker, H.; Smolka, M.; Keßler, A.; Leineweber, A.; Wolf, G. Intermetallic Sludge Formation in Fe Containing Secondary Al-Si Alloys Influenced by Cr and Mn as Preparative Tool for Metal Melt Filtration. *Adv. Eng. Mater.* **2017**, *19*, 1700161. [[CrossRef](#)]
- Becker, H.; Thum, A.; Distl, B.; Kriegel, M.J.; Leineweber, A. Effect of melt conditioning on removal of Fe from secondary Al-Si alloys containing Mg, Mn, and Cr. *Met. Mater. Trans. A* **2018**, *49*, 6375–6389. [[CrossRef](#)]
- Que, Z.; Mendis, C.L. Heterogeneous nucleation and phase transformation of Fe-rich intermetallic compounds in Al-Mg-Si alloys. *J. Alloys Compd.* **2020**, *836*, 155515. [[CrossRef](#)]
- Bjurenstedt, A.; Casari, D.; Seifeddine, S.; Mathiesen, R.H.; Dahle, A.K. In-situ study of morphology and growth of primary α -Al(FeMnCr)Si intermetallics in an Al-Si alloy. *Acta Mater.* **2017**, *130*, 1–9.
- Simensen, C.J.; Bjorneklett, A. A Model for α -Al(Mn, Fe)Si Crystals. In *Light Metals 2017; The Minerals, Metals & Materials Society; Springer International Publishing: San Diego, CA, USA, 2017; pp. 197–203.*
- Yu, J.; Wanderka, N.; Rack, A.; Daudin, R.; Boller, E.; Markötter, H.; Manzoni, A.; Vogel, F.; Arlt, T.; Manke, I.; et al. Influence of impurities, strontium addition and cooling rate on microstructure evolution in Al-10Si-0.3Fe casting alloys. *J. Alloys Compd.* **2018**, *766*, 818–827. [[CrossRef](#)]
- Kakitani, R.; Rodrigues, A.V.; Silva, C.; Garcia, A.; Cheung, N. The roles of solidification cooling rate and (Mn, Cr) alloying elements in the modification of β -AlFeSi and hardness evolvments in near-eutectic Al-Si alloys. *J. Alloys Metall. Syst.* **2023**, *1*, 100005. [[CrossRef](#)]
- Barlock, J.G.; Mondolfo, L.F. Structure of Some Aluminium-Iron-Magnesium-Manganesesilicon Alloys. *Z. Fur Met.* **1975**, *66*, 605.
- Crepeau, P.N. Effect of iron in Al-Si casting alloys: A critical review. *AFS Trans.* **1995**, *103*, 361–366.
- Narayanan, L.A.; Samuel, F.H.; Gruzleski, J.E. Crystallization behavior of iron-containing intermetallic compounds in 319 aluminum alloy. *Met. Mater. Trans. A* **1994**, *25*, 1761–1773. [[CrossRef](#)]
- Narayanan, L.A.; Samuel, F.H.; Gruzleski, J.E. Dissolution of iron intermetallics in Al-Si alloys through Nonequilibrium Heat Treatment. *Metall. Mater. Trans. A* **1995**, *26*, 2161–2173. [[CrossRef](#)]
- Dash, S.S.; Chen, D. A Review on Processing–Microstructure–Property Relationships of Al-Si Alloys: Recent Advances in Deformation Behavior. *Metals* **2023**, *13*, 609. [[CrossRef](#)]
- Efzan, M.N.E.; Kong, H.; Kok, C. Review: Effect of Alloying Element on Al-Si Alloys. *Adv. Mater. Res.* **2013**, *845*, 355–359. [[CrossRef](#)]

20. Ammar, H.R.; Moreau, C.; Samuel, A.M.; Samuel, F.H.; Doty, H.W. Influences of alloying elements, solution treatment time and quenching media on quality indices of 413-type Al–Si casting alloys. *Mater. Sci. Eng. A* **2008**, *489*, 426–438. [[CrossRef](#)]
21. Ou, L.; Xing, S.; Sun, H.; Yan, G. Effect of Simultaneous Mg and Zn Addition on the Solidification and Microstructure of Multi-Element Hypoeutectic Al–Si Alloys. *Met. Mater. Int.* **2024**, 1–18. [[CrossRef](#)]
22. Zhang, L.; Chen, S.; Li, Q.; Chang, G. Formation mechanism and conditions of fine primary silicon being uniformly distributed on single α Al matrix in Al–Si alloys. *Mater. Des.* **2020**, *193*, 108853. [[CrossRef](#)]
23. Qiao, H.; Gao, T.; Zhu, X.; Wu, Y.; Qian, Z.; Liu, X. Generation and evolution of nanoscale AlP and Al₁₃Fe₄ particles in Al–Fe–P system. *J. Alloys Compd.* **2015**, *622*, 662–668. [[CrossRef](#)]
24. Ludwig, T.H.; Schaffer, P.L.; Arnberg, L. Influence of phosphorus on the nucleation of eutectic silicon in Al–Si alloys. *Met. Mater. Trans. A* **2013**, *44*, 5796–5805. [[CrossRef](#)]
25. Zheng, Z.-K.; Mao, W.-M.; Liu, Z.-Y.; Wang, D.; Yue, R. Refinement of primary Si grains in Al–20%Si alloy slurry through serpentine channel pouring process. *Int. J. Miner. Met. Mater.* **2016**, *23*, 572–580. [[CrossRef](#)]
26. Sun, J.; Zhang, L.; Wu, G.; Liu, W.; Hu, Z.; Chen, A. Refinement of primary Si in Al–20%Si alloy by MRB through phosphorus additions. *J. Mater. Process. Technol.* **2015**, *225*, 485–491. [[CrossRef](#)]
27. Bobel, A.; Kim, K.; Wolverton, C.; Walker, M.; Olson, G.B. Equilibrium composition variation of Q-phase precipitates in aluminum alloys. *Acta Mater.* **2017**, *138*, 150–160. [[CrossRef](#)]
28. Alyaldin, L.; Abdelaziz, M.H.; Samuel, A.M.; Doty, H.W.; Valtierra, S.; Samuel, F.H. Effects of Alloying Elements and Testing Temperature on the Q-Index of Al–Si Based Alloys. *Int. J. Met.* **2018**, *12*, 839–852. [[CrossRef](#)]
29. Yıldırım, M.; Özyürek, D. The effects of Mg amount on the microstructure and mechanical properties of Al–Si–Mg alloys. *Mater. Des.* **2013**, *51*, 767–774. [[CrossRef](#)]
30. Hao, J.; Yu, B.; Bian, J.; Chen, B.; Wu, H.; Li, W.; Li, Y.; Li, R. Calculation Based on the Formation of Mg₂Si and Its Effect on the Microstructure and Properties of Al–Si Alloys. *Materials* **2021**, *14*, 6537. [[CrossRef](#)] [[PubMed](#)]
31. Ružbarský, J. *Al–Si Alloys Casts by Die Casting*; Springer Briefs in Applied Sciences and Technology; Springer: Cham, Switzerland, 2019. [[CrossRef](#)]
32. *ASTM B-108*; Standard Specification for Aluminum-Alloy Permanent Mold Castings. ASTM: West Conshohocken, PA, USA, 2021.
33. Bolzoni, L.; Nowak, M.; Babu, N.H. Grain refinement of Al–Si alloys by Nb–B inoculation. Part II: Application to commercial alloys. *Mater. Des.* **2015**, *66*, 376–383. [[CrossRef](#)]
34. Shabani, M.; Emamy, M.; Nemati, N. Effect of grain refinement on the microstructure and tensile properties of thin 319 Al castings. *Mater. Des.* **2011**, *32*, 1542–1547. [[CrossRef](#)]
35. Samuel, E.; Golbahar, B.; Samuel, A.M.; Doty, H.W.; Valtierra, S.; Samuel, F.H. Effect of grain refiner on the tensile and impact properties of Al–Si–Mg cast alloys. *Mater. Des.* **2014**, *56*, 468–479.
36. Samuel, E.; Tahiri, H.; Samuel, A.M.; Songmene, V.; Samuel, F.H. A Review on Fundamentals of Grain Refining of Al–Si Cast Alloys [Internet]. Recent Advancements in Aluminum Alloys. IntechOpen. 2024. Available online: <https://www.intechopen.com/chapters/88361> (accessed on 29 December 2024).
37. Sunitha, K.; Gurusami, K. Study of Al–Si alloys grain refinement by inoculation. *Mater. Today Proc.* **2021**, *43*, 1825–1829.
38. Nadendla, H.B.; Nowak, M.; Bolzoni, L. Grain Refiner for Al–Si Alloys. In *Light Metals 2013*; Sadler, B.A., Ed.; The Minerals, Metals & Materials Series; Springer: Cham, Switzerland, 2016. [[CrossRef](#)]
39. Vandersluis, E.; Emadi, P.; Andilab, B.; Ravindran, C. The Role of Silicon Morphology in the Electrical Conductivity and Mechanical Properties of As-Cast B319 Aluminum Alloy. *Met. Mater. Trans. A* **2020**, *51*, 1874–1886. [[CrossRef](#)]
40. Shen, Y.; Liu, X.-S.; He, G.-Q.; Tian, D.-D.; Wang, Q.-G.; Lv, S.-Q. Quantitative microstructure and fatigue life of B319 casting alloys. *Rare Met.* **2017**, *36*, 780–791. [[CrossRef](#)]
41. Mohamed, A.M.A.; Ibrahim, M.F.; Samuel, E.; Samuel, A.M.; Samuel, F.H.; Doty, H.W. Assessment of the Effect of Mg Addition on the Solidification Behavior, Tensile and Impact Properties of Al–Si–Cu Cast Alloys. *Int. J. Met.* **2022**, *17*, 82–108. [[CrossRef](#)]
42. Basak, C.B.; Babu, N.H. Influence of Cu on modifying the beta phase and enhancing the mechanical properties of recycled Al–Si–Fe cast alloys. *Sci. Rep.* **2017**, *7*, 5779. [[CrossRef](#)]
43. Liu, X.; Wang, C.; Zhang, S.-Y.; Song, J.-W.; Zhou, X.-L.; Zha, M.; Wang, H.-Y. Fe-bearing phase formation, microstructure evolution, and mechanical properties of Al–Mg–Si–Fe alloy fabricated by the twin-roll casting process. *J. Alloys Compd.* **2021**, *886*, 161202. [[CrossRef](#)]
44. Epifano, E.; Monceau, D. Ellingham diagram: A new look at an old tool. *Corros. Sci.* **2023**, *217*, 111113. [[CrossRef](#)]
45. Tian, N.; Wang, G.; Zhou, Y.; Liu, C.; Liu, K.; Zhao, G.; Zuo, L. Formation of Phases and Microstructures in Al–8Si Alloys with Different Mg Content. *Materials* **2021**, *14*, 762. [[CrossRef](#)]
46. Eisaabadi, B.G.; Davami, P.; Kim, S.K.; Varahram, N. Effects of hydrogen and oxides on tensile properties of Al–Si–Mg cast alloys. *Mater. Sci. Eng. A* **2012**, *552*, 36–47.
47. Eisaabadi, B.G.; Davami, P.; Kim, S.K.; Varahram, N.; Yoon, Y.O.; Yeom, G.Y. Effect of oxide films, inclusions and Fe on reproducibility of tensile properties in cast Al–Si–Mg alloys: Statistical and image analysis. *Mater. Sci. Eng. A* **2012**, *558*, 134–143.

48. Zhang, B.R.; Zhang, L.K.; Wang, Z.M.; Gao, A.J. Achievement of High Strength and Ductility in Al–Si–Cu–Mg Alloys by Intermediate Phase Optimization in As-Cast and Heat Treatment Conditions. *Materials* **2020**, *13*, 647. [[CrossRef](#)]
49. Yigezu, B.S.; Mahapatra, M.M.; Jha, P.K. Influence of Reinforcement Type on Microstructure, Hardness, and Tensile Properties of an Aluminum Alloy Metal Matrix Composite. *J. Miner. Mater. Charact. Eng.* **2013**, *1*, 33948. [[CrossRef](#)]
50. Toschi, S. Optimization of a354 Al-Si-Cu-Mg alloy heat treatment: Effect on microstructure, hardness, and tensile properties of peak aged and overaged alloy. *Metals* **2018**, *8*, 961. [[CrossRef](#)]
51. Peng, H.P.; Zhi, W.L.; Zhu, J.Q.; Su, X.P.; Liu, Y.; Wu, C.J.; Wang, J.H. Microstructure and mechanical properties of Al–Si alloy modified with Al–3P. *Trans. Nonferrous Met. Soc. China* **2020**, *30*, 595–602.
52. Kumar, G.B.V.; Rao, C.S.P.; Selvaraj, N. Mechanical and Tribological Behaviour of Particulate Reinforced Aluminium Metal Matrix Composites—A Review. *J. Miner. Mater. Charact. Eng.* **2011**, *10*, 59–91.
53. Sahin, I.; Eker, A.A. Analysis of Microstructures and Mechanical Properties of Particle Reinforced AlSi7Mg2 Matrix Composite Materials. *J. Mater. Eng. Perform.* **2011**, *20*, 1090–1096. [[CrossRef](#)]
54. Campbell, J.; Tiryakioğlu, M. Review of effect of P and Sr on modification and porosity development in Al–Si alloys. *Mater. Sci. Technol.* **2010**, *26*, 262–268. [[CrossRef](#)]
55. De Giovanni, M.; Kaduk, J.A.; Srirangam, P. Modification of Al-Si Alloys by Ce or Ce with Sr. *JOM* **2019**, *71*, 426–434. [[CrossRef](#)]
56. Gao, T.; Hu, J.; Li, M.; Li, C.; Su, H.; Liu, J.; Liu, X. On the formation of Al₂Si₂Sr phase and its behavior in Al–Si–Sr alloys. *J. Alloys Compd.* **2024**, *985*, 174023. [[CrossRef](#)]
57. Barrirero, J.; Li, J.; Engstler, M.; Ghafoor, N.; Schumacher, P.; Odén, M.; Mücklich, F. Cluster formation at the Si/liquid interface in Sr and Na modified Al–Si alloys. *Scr. Mater.* **2016**, *117*, 16–19. [[CrossRef](#)]
58. Drouzy, M.; Jacob, S.; Richard, M. Interpretation of Tensile Results by Means of Quality Index and Probable Yield Strength. *AFS Int. Cast Met. J.* **1980**, *5*, 43–50.
59. Jacob, S. Quality Index in Predicting of Properties of Aluminum Castings-A Review. *AFS Trans.* **2000**, *108*, 811–818.

Disclaimer/Publisher’s Note: The statements, opinions and data contained in all publications are solely those of the individual author(s) and contributor(s) and not of MDPI and/or the editor(s). MDPI and/or the editor(s) disclaim responsibility for any injury to people or property resulting from any ideas, methods, instructions or products referred to in the content.